ELSEVIER

Journal of Fluids and Structures 23 (2007) 207–226

JOURNAL OF FLUIDS AND STRUCTURES

www.elsevier.com/locate/jfs

Numerical simulation of flow around a square cylinder in uniform-shear flow

M. Cheng*, D.S. Whyte, J. Lou

Institute of High Performance Computing, 1 Science Park Road, #01-01 The Capricorn, Singapore Science Park II, Singapore 117528, Singapore

Received 5 December 2005; accepted 11 August 2006
Available online 25 October 2006

Abstract

This paper presents results obtained from a numerical simulation of a two-dimensional (2-D) incompressible linear shear flow over a square cylinder. Numerical simulations are performed, using the lattice Boltzmann method, in the ranges of $50 \leqslant Re \leqslant 200$ and $0 \leqslant K \leqslant 0.5$, where Re and K are the Reynolds number and the shear rate, respectively. The effect of the shear rate on the frequency of vortex shedding from the cylinder, and the lift and drag forces exerted on the cylinder are quantified together with the flow patterns around the cylinder. The present results show that vortex structure behind the cylinder is strongly dependant on both the shear rate and Reynolds number. When $Re = 50$, a small K can disturb the steady state and cause an alternative vortex shedding with uneven intensity. In contrast, a large value of K will suppress the vortex shedding from the cylinder. When $Re > 50$, the differences in the strength and size of vortices shed from the upper and lower sides of the cylinder become more pronounced as K increases. Vortex shedding disappears when K is larger than a critical value, which depends on Re. The flow patterns around the cylinder for different Re tend towards self-similarity with increasing K. The lift and drag forces exerted on the cylinder, in general, decrease with increasing K. Unlike a shear flow past a circular cylinder, the vortex shedding frequency past a square cylinder decreases with increasing the shear rate. A significant reduction of the drag force occurs in the range $0.15 < K < 0.3$.

Keywords: Shear flow; Square cylinder; Vortex street; Lattice Boltzmann method

1. Introduction

The study of uniform flow past a cylindrical obstacle has fascinated researchers for a long time, and detailed information is available in the literature. However, many practical cases exist where the flow approaching a body is sheared rather than uniform. For example, cylindrical structures submerged in wind, tides or currents are always exposed to a nonuniform free stream. When the oncoming free stream is a linear flow, a constant vorticity is embedded in the free stream. This may lead to a complicated interaction with the boundary layers that separate from the body which results in a different type of vortex shedding structure. Vortex shedding has often been the cause of flow-induced structure failure. It is important to know the effects of the approaching shear flow on the mechanism of vortex

*Corresponding author. Tel.: +65 6419 1276; fax: +65 6419 1580.
E-mail address: chengm@ihpc.a-star.edu.sg (M. Cheng).

0889-9746/$ - see front matter © 2006 Elsevier Ltd. All rights reserved.
doi:10.1016/j.jfluidstructs.2006.08.011

shedding. Such a study would lead to better understanding of the vortex-induced vibration, its subsequent suppression and control (Zhou et al., 2005).

Although a large number of studies with a uniform flow stream exist, there has been relatively little work carried out to investigate the shear flow problem. Only a few experimental and numerical studies on shear flow past a circular cylinder have been conducted in the past. Kiya et al. (1980) experimentally investigated vortex shedding frequency of a circular cylinder in a linear shear flow and the flow patterns around the cylinder. The Reynolds number (defined in terms of the cylinder diameter and the approaching velocity at its centre) ranged from 35 to 1500. The shear parameter K (the transverse velocity gradient of the shear flow nondimensionalized by the cylinder diameter and the approaching velocity at its centre) was varied from 0 to 0.25. They found that the critical Reynolds number for the onset of vortex shedding from the cylinder is higher for shear flow than that for a uniform stream. The critical Reynolds number also increases approximately linearly with increasing shear parameter when the latter was larger than about 0.06. For cases where the Reynolds number is in the range of 43–220, the vortex shedding disappears for sufficiently large shear parameters. Kiya et al. (1980) also examined the Strouhal number (i.e. dimensionless group combining obstacle length scale, imposed flow field velocity and the frequency of vortex shedding). It was found that in the range of $100 < \mathrm{Re} < 1000$, the Strouhal number increases as the shear parameter is larger than 0.1. In the same range of shear parameter as that studied by Kiya et al. (1980), Kwon et al. (1992) used an image processing visualization to investigate linear shear flow past a circular cylinder at higher Reynolds numbers ($600 \leqslant \mathrm{Re} \leqslant 1600$). They verified that the Strouhal number increases rapidly with Reynolds number at small values of Re. However, in the range of $400 \leqslant \mathrm{Re} \leqslant 700$, the Strouhal number reaches a nearly constant value of approximately 0.22. In general, the Strouhal number increases as the shear parameter increases. The scatter in data was appreciably smaller in their experiments than in that of Kiya et al. (1980). The drag coefficient tends to decrease with either increasing Re or increasing shear parameter.

Following the Kwon et al. work, an expanded experimental work was carried out by Sung et al. (1995) using laser-Doppler velocity measurements to describe the wake characteristics of the linear shear flow past a rotating cylinder. The Reynolds number and the shear parameter realized in their experiment were in the ranges of $600 \leqslant \mathrm{Re} \leqslant 1200$, $0 \leqslant \mathrm{K} \leqslant 0.15$. The ratio of the peripheral linear speed of the cylinder to the centreline free-stream speed varied from -2 to 2. The power spectra of velocity measurements at downstream locations were analysed to determine the vortex shedding patterns. It was found that the dominant shedding frequency is shifted towards a higher value as the rotation velocity and K increase. When the cylinder rotation velocity increases beyond a certain threshold value, the dominant frequency becomes less distinct.

A numerical investigation on a linear shear flow past a circular cylinder was carried out by Jordan and Fromm (1972), for $\mathrm{K} = 0.05$ and $\mathrm{Re} = 400$. Due to the very small value for K, Jordan and Fromm (1972) found that at this small value of $\mathrm{K} = 0.05$, the Strouhal number of vortex shedding in this weak shear flow is the same in magnitude as the corresponding uniform flow Strouhal number ($\mathrm{St} = 0.2$). Ayukawa et al. (1993) performed numerical simulation of a shear flow past a square cylinder for a high Reynolds number of 4000. They used a discrete vortex model to study the effects of the shear rate on the Strouhal number and the force acting on the cylinder for $\mathrm{K} \leqslant 0.15$. Their results showed that, within the extent of their simulation, the shear rate effects are fairly small on the vortex shedding frequency, while the flow pattern is affected strongly by the shear rate.

However, the common points of interest of these investigations are how the Strouhal number varies with the shear parameter and Reynolds number. The vortex shedding mechanism and flow structure in a shear flow are still not fully understood. Recently, Cheng et al. (2005) used a lattice Boltzmann method to investigate a low Reynolds number linear shear flow past a square cylinder. Their results show that the vortex structure behind the cylinder is strongly shear-rate dependent. However, the study was limited to a single Reynolds number. It is well known that the vortex shedding phenomenon can be dramatically altered for uniform flows past a bluff body at different Reynolds numbers. Naturally, the vortex structure behind the cylinder in shear flow may also be Reynolds-number dependent.

In this paper, a linear shear flow past a square cylinder (Fig. 1) is studied systematically over a range of shear rates at different Reynolds numbers by making use of an efficient numerical scheme. This work has been motivated by the need to better understand the effect of shear flow on the vortex structure behind a square cylinder. A practical situation when the vortex structure play an important role is in the interaction between fluid flow and a cylindrical prism in the atmospheric boundary layer. The shear parameter K is defined as $\mathrm{K} = \tilde{G}\tilde{a}/\tilde{U}_c$, where $\tilde{G}$ is the dimensional velocity gradient, $\tilde{a}$ is the side length of the cylinder and $\tilde{U}_c$ is the velocity on the symmetry axis of the cylinder far upstream. The Reynolds number is based on $\tilde{a}$ and $\tilde{U}_c$, respectively.

The lattice Boltzmann method, which was previously developed and applied to the simulation of a large-gradient flow (Cheng and Hung, 2004, 2006; Cheng et al., 2005), is also used for the present numerical simulation. This study will shed light on the development of a periodic pattern of vortex shedding associated with the Kármán vortex street behind the cylinder at different K and Re. Some other important aspects, such as the relation between the Strouhal number and the shear parameter K, the pressure distributions around the cylinder, as well as the forces acting on it at different shear parameters, will also been investigated by the numerical simulations.

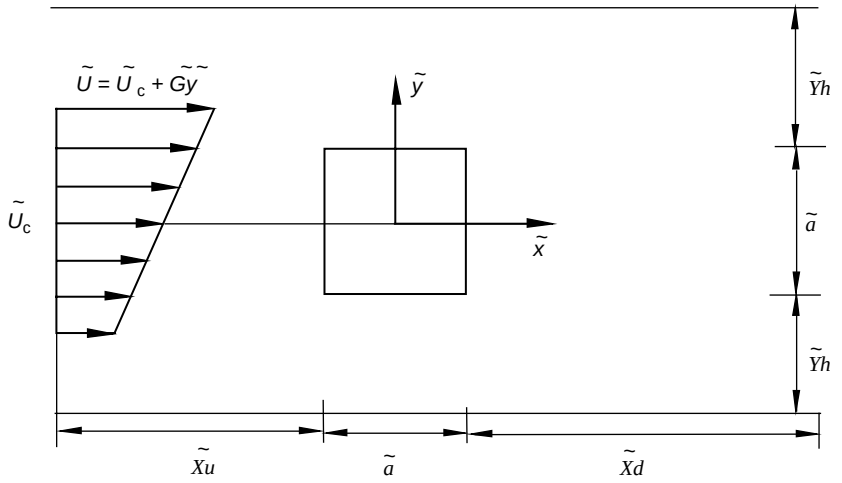

Fig. 1. Schematic of the flow configuration, coordinate system.

2. Numerical method

The lattice Boltzmann method (LBM) is an alternative to conventional computational fluid dynamics methods for solving Navier–Stokes equations (Higuera and Jimenez, 1989; Higuera et al., 1989; Benzi et al., 1992; Chen and Doolen, 1998). It is based on microscopic models and a mesoscopic kinetic equation for the particle distribution function. Unlike traditional numerical methods which solve the macroscopic variables such as velocity and density directly, these variables are obtained in LBM by moment integrations of the particle distribution function. Therefore, the LBM has several computational advantages, i.e., higher precision, simplicity of programming, intrinsic parallelism of the algorithm and data structure. Additionally, traditional CFD solvers typically require a velocity–pressure correction step (for mass conservation) involving the global solution of the Poisson equation. For LBM, there is no requirement to solve this Poisson equation, and the pressure is a local variable (Rossi et al., 2005).

2.1. Lattice Boltzmann equation

The Boltzmann equation with the Bhatnagar–Gross–Krook (BGK) approximation for the particle collision operator (Bhatnagar et al., 1954) is based on the premise that a particle distribution will relax to a final state given by the Maxwell–Boltzmann equilibrium distribution at a rate inversely proportional to the relaxation time, $\tilde{\tau}$. The BGK Boltzmann equation is

$$\frac{\partial \tilde{f}}{\partial \tilde{t}} + \tilde{c} \cdot \nabla \tilde{f} = -\frac{\tilde{f} - \tilde{f}^{eq}}{\tilde{\tau}}, \tag{1}$$

where $\tilde{f}$ is the single-particle velocity distribution function, $\tilde{t}$ is the time, $\tilde{c}$ is the microscopic velocity, and $\tilde{f}^{eq}$ is the equilibrium distribution function (external forces have been neglected). Macroscopic fluid variables, such as the density ($\tilde{\rho}$) and velocity ($\tilde{u}$), can be calculated by the integration of the distribution function $\tilde{f}$,

$$\tilde{\rho} = \int \tilde{f}(\tilde{r}, \tilde{c}, \tilde{t})\, d\tilde{c}, \tag{2}$$

$$\tilde{\rho}\tilde{u} = \int \tilde{c}\, \tilde{f}(\tilde{r}, \tilde{c}, \tilde{t})\, d\tilde{c}. \tag{3}$$

When the physical space is divided into a regular lattice and the velocity space is defined by a set of finite, discrete velocities $\{\tilde{c}_\alpha\}$, the lattice version of Eq. (1) can be written as

$$\frac{\partial \tilde{f}_\alpha}{\partial \tilde{t}} + \tilde{c}_\alpha \cdot \nabla \tilde{f}_\alpha = -\frac{\tilde{f}_\alpha - \tilde{f}^{eq}_\alpha}{\tilde{\tau}}, \tag{4}$$

where $\tilde{f}_\alpha$ and $\tilde{f}_\alpha^{eq}$ are the single-particle velocity distribution function and the equilibrium distribution along the α direction, respectively.

Eq. (4) is nondimensionalized by the cylinder side length ($\tilde{a}$), the reference speed ($\tilde{U}_c$), density ($\tilde{\rho}_0$), and the time between particle collisions ($\tilde{t}_c$),

$$\frac{\partial f_\alpha}{\partial t} + c_\alpha \cdot \nabla f_\alpha = -\frac{f_\alpha - f_\alpha^{eq}}{\varepsilon\tau}. \tag{5}$$

Nondimensional variables are defined according to

$$c_\alpha = \frac{\tilde{c}_\alpha}{\tilde{U}_c}, \quad \nabla = \tilde{a}\tilde{\nabla}, \quad f_\alpha = \frac{\tilde{f}_\alpha}{\tilde{\rho}_0}, \quad t = \frac{\tilde{t}\tilde{U}_c}{\tilde{a}}, \quad \tau = \frac{\tilde{\tau}}{\tilde{t}_c}, \quad r = \frac{\tilde{r}}{\tilde{a}}, \quad \varepsilon = \frac{\tilde{t}_c\tilde{U}_c}{\tilde{a}}, \tag{6}$$

where the dimensional variables are denoted with a tilde. The variable ε may be interpreted as either the ratio of collision time to flow time or as the ratio of mean free path to the characteristic length (i.e. Knudsen number).

Eq. (5) is discretized in time and space as follows:

$$\frac{f_\alpha(r,t+\Delta t) - f_\alpha(r,t)}{\Delta t} + \frac{f_\alpha(r+\Delta x, t+\Delta t) - f_\alpha(r,t+\Delta t)}{\Delta x}c_{\alpha x} + \frac{f_\alpha(r+\Delta y, t+\Delta t) - f_\alpha(r,t+\Delta t)}{\Delta y}c_{\alpha y} = -\frac{f_\alpha(r,t) - f_\alpha^{eq}(r,t)}{\tau\varepsilon}. \tag{7}$$

Choosing $c_\alpha = \Delta r/\Delta t$ and $\tilde{t}_c = \Delta\tilde{t}$, we obtain

$$f_\alpha(r + c_\alpha\Delta t, t+\Delta t) = f_\alpha(r,t) - \frac{f_\alpha(r,t) - f_\alpha^{eq}(r,t)}{\tau}. \tag{8}$$

Eq. (8) governs the evolution of microscopic mass, and is commonly referred to as the LBM.

The present study examines two-dimensional (2D) flow, and a 2D square lattice with nine velocities (D2Q9 model) is used. These nine velocities are

$$c_\alpha = ce_\alpha = \begin{cases} (0,0) & \alpha = 0, \\ c\left[\cos\left(\frac{\alpha-1}{2}\pi\right), \sin\left(\frac{\alpha-1}{2}\pi\right)\right] & \alpha = 1,2,3,4, \\ \sqrt{2}c\left[\cos\left(\frac{\alpha-5}{2}\pi + \frac{\pi}{4}\right), \sin\left(\frac{\alpha-5}{2}\pi + \frac{\pi}{4}\right)\right] & \alpha = 5,6,7,8, \end{cases} \tag{9}$$

where $c = \Delta x/\Delta t$, Δx being the lattice constant. The equilibrium distribution function for this model is

$$f_\alpha^{eq} = \rho w_\alpha\left[1 + \frac{3}{c^2}c_\alpha \cdot u + \frac{9}{2c^4}(c_\alpha \cdot u)^2 - \frac{3}{2c^2}u \cdot u\right] \quad \alpha = 0,1,2,\ldots,8, \tag{10}$$

where $w_0 = 4/9$, $w_1 = w_2 = w_3 = w_4 = 1/9$, and $w_5 = w_6 = w_7 = w_8 = 1/36$. The pressure (p) is determined by the isothermal equation of state,

$$p = \rho c_s^2, \tag{11}$$

where c_s is the nondimensional lattice sound speed, and is equal to $1/\sqrt{3}$ in this model (Wolf-Gladrow, 2000). In the discretized velocity space, the macroscopic quantities, ρ and u, are calculated from

$$\rho = \sum_{\alpha=0}^{8} f_\alpha \quad \text{and} \quad \rho u = \sum_{\alpha=0}^{8} f_\alpha c_\alpha. \tag{12}$$

2.2. The macroscopic equations

Using the Chapman–Enskog expansion (Chapman and Cowling, 1970), one can obtain following equations from Eq. (8):

$$\frac{\partial\rho}{\partial t} + \nabla \cdot (\rho u) = 0 \tag{13}$$

and

$$\rho\left[\frac{\partial u}{\partial t}+(u\cdot\nabla)u\right]=-\nabla p+\nabla\cdot\Pi, \tag{14}$$

where

$$\Pi=\chi\left(\frac{\rho}{3}\left(\frac{\partial u_j}{\partial x_i}+\frac{\partial u_i}{\partial x_j}\right)-\frac{\partial\rho u_i u_j u_k}{\partial x_k}\right),\quad i,j,k=1,2, \tag{15}$$

$$\chi=\left(\tau-\frac{1}{2}\right)\Delta t. \tag{16}$$

For incompressible flow, $|u|/c_s\ll 1$, if the term $\left(\partial\rho u_i u_j u_k/\partial x_k\right)$ is ignored, Eq. (14) turns out to have exactly the same form as the incompressible Navier–Stokes equations. The corresponding kinematic viscosity (v) in the Navier–Stokes equations derived from Eq. (8) is

$$v=\left(\frac{2\tau-1}{6}\right)\Delta t. \tag{17}$$

2.3. Numerical implementation

The LBM belongs to a class of the pseudo-compressible solvers of the Navier–Stokes equations for incompressible flow. In order to correctly simulate the incompressible flow in practice, one must ensure that the Mach number, $M=\tilde{U}_c/\tilde{c}_s\ll 1$. Since $\tilde{c}_s$ is a constant in the LBM, the restriction on M requires that the velocity $\tilde{U}_c$ be sufficiently small. In order to maintain the Mach number and Knudsen number in the suitable ranges ($M\ll 1$ and $Kn<0.01$) it is necessary to limit the velocity $\tilde{U}_c$ to between 0.01 and 0.04. As the viscosity of the fluid is specified to be $v=0.01$, the Reynolds number range for the present study is 50–200.

In standard LBM, the algorithm is constructed on a special class of uniform and regular lattices. Eq. (8) can be solved in two steps, i.e., a collision step, followed by a streaming step. The collision step is locally defined because the equilibrium distribution depends only on the local values of mass and momentum density. The streaming step is uniform and requires little computational effort when the computational mesh coincides with the lattice. However, the use of a uniform lattice as a computational mesh is quite restrictive in many applications; for instance, where a large gradient exists only in a small region of the computational domain.

In order to improve the computational efficiency, LBM was extended to nonuniform grids (Nannelli and Succi, 1992; Cheng and Hung, 2004), and the computational mesh is decoupled from the lattice. In the approach of Cheng and Hung (2004), a particle initially located at the grid point A(x, y), will stream to the position $A'(x+c_{\alpha x}\Delta t,\ y+c_{\alpha y}\Delta t)$ after one time step, Δt, along the α direction. For a lattice mesh, A′ is at the grid point. However, A′ is usually not at the mesh point when the mesh is decoupled from the lattice. However, in the numerical simulation, one is only interested in the distribution function at the mesh point. In the modified LBM used here, the following Lagrange interpolation is adopted to get the distribution function at the nonuniform mesh point at time $t+\Delta t$. Therefore, Eq. (8) can be solved on the nonuniform mesh in the following three steps:

collision step:

$$f_\alpha^*(r,t)=f_\alpha(r,t)-\frac{f_\alpha(r,t)-f_\alpha^{eq}(r,t)}{\tau}, \tag{18}$$

streaming step:

$$f_\alpha^{**}(r+c_\alpha\Delta t,t+\Delta t)=f_\alpha^*(r,t), \tag{19}$$

interpolation step:

$$f_\alpha(r,t+\Delta t)=\sum_{m=1}^{3}\sum_{n=1}^{3}\prod_{\substack{p=1\\p\neq m}}^{3}\frac{x-x_p}{x_m-x_p}\prod_{\substack{q=1\\q\neq n}}^{3}\frac{y-y_q}{y_n-y_q}f_\alpha^{**}. \tag{20}$$

The above scheme had earlier been used for the simulations of a square cavity flow and flow past a circular cylinder. The results showed that when the maximum mesh size to lattice size ratio δ is limited below 5, a satisfactory accuracy can be achieved in the flow simulation. The details of errors, convergence and mesh effect on the result were discussed by Cheng and Hung (2004) and He et al. (1996).

Table 1
Comparison of lift and drag coefficients and Strouhal number at K = 0

	Re = 100			Re = 200		
	St	$\bar{C}_D$	$\bar{C}_{Lrms}$	St	$\bar{C}_D$	$\bar{C}_{Lrms}$
Okajima (1982)	0.135–0.140	—	—	0.14–0.148	1.45	—
Jan and Sheu (2004)	0.140	—	—	0.148	—	—
Davis and Moore (1982)	0.154	1.64	—	—	—	—
Sohankar et al. (1998)	0.146	1.47	0.156	0.15	1.462	0.377
Present	0.144	1.44	0.152	0.15	1.45	0.372

In the present study, the total computation domain is a rectangle of size $(\tilde{X}u + \tilde{a} + \tilde{X}d)(2\tilde{Y}h + \tilde{a})$, as shown in Fig. 1. The flow-field considered here is surrounded by an inflow boundary at the left, a free outflow boundary at the right, and the upper and lower free-slip boundaries. The inflow boundary condition is

$$f_\alpha = f_\alpha^{eq}\big|_{\tilde{u}=\tilde{U}}. \tag{21}$$

At the outflow boundary, owing to the extremely large domain behind the cylinder, no influence is expected for the results, and a fixed pressure is imposed in terms of the equilibrium distribution function at the outlet. For this task, the velocity components are extrapolated downstream (Succi, 2001; Ansumali et al., 2004). A no-slip condition is applied at the surface of the cylinder. This is implemented in LBM via a 'bounce-back' rule, in which all particles hitting a wall are reflected back in the direction from which they came (Ziegler, 1993). Although this rule has errors in velocity at the wall (Noble et al., 1995; Inamuro et al., 1995), it does provide reasonably accurate flow solutions for a range of discretization parameters. When $\tau < 2$, the second-order accuracy for the non-slip condition can be achieved if the wall is placed in the middle of the lattice nodes (Ladd, 1994). In the present paper, $\tau = 0.53$ and the wall is placed in the middle of the lattice nodes, so the influence of the slip velocity on the results can be ignored (Gallivan et al., 1997; He et al., 1997).

In this paper, $\tilde{X}u = 12\tilde{a}$, $\tilde{X}d = 30\tilde{a}$, $\tilde{Y}h = 12\tilde{a}$ and the nonuniform mesh $\delta = 4$ and $I \times J = 1000 \times 600$ (where I and J are the number of points in the x and y direction, respectively) are adopted. The choice of the mesh structure has been discussed and justified in our previous work (Cheng et al., 2005). A comparison between the results reported by other investigators and the present computation on the nonuniform mesh at K = 0 is given in Table 1, which shows generally close agreement.

The Strouhal number, pressure (C_P), lift (C_L) and drag (C_D) coefficients are defined as

$$St = \frac{\tilde{f}\tilde{a}}{\tilde{U}_c}, \tag{22}$$

$$C_P = \frac{2\tilde{p} - \tilde{p}_0}{\tilde{\rho}_0 \tilde{U}_c^2}, \tag{23}$$

$$C_L = \frac{2\tilde{F}_L}{\tilde{\rho}_0 \tilde{U}_c^2 \tilde{a}}, \tag{24}$$

$$C_D = \frac{2\tilde{F}_D}{\tilde{\rho}_0 \tilde{U}_c^2 \tilde{a}}, \tag{25}$$

where $\tilde{f}$,$\tilde{p}$, $\tilde{F}_L$ and $\tilde{F}_D$ are the period of vortex shedding, the pressure, the lift, and the drag exerted by the fluid on a unit length of the cylinder, respectively. The reference pressure is $\tilde{p}_0$.

3. Results and discussion

The detailed calculations of the shear flow past a square cylinder are carried out at Reynolds number Re = 50, 100 and 200. The shear rate K varies from 0 to 0.5.

3.1. Flow features

The effects of shear rate on the structure of the wake flow behind the cylinder are described in Figs. 2–4 for different Reynolds numbers. Fig. 2 shows the patterns of instantaneous streaklines for Re = 50. When K = 0 (Fig. 2(a)), the flow pattern is symmetric with respect to the oncoming flow and there is a closed recirculation zone behind the cylinder. This zone is made up of two symmetrical vortices that rotate in opposite directions. Owing to the sharp corners, the separation point is fixed at the trailing edge and the flow is attached at the side walls. There is no vortex shedding in the wake.

When $K>0$, the shear gradient in the boundary layer on the surface of the cylinder becomes asymmetrical at the start of the motion since the relative velocities of the fluid with respect to the wall are, respectively, $1+K/2$ and $1-K/2$ on the upper and lower sides of the cylinder. The flow separation induces asymmetrical vortices. Initial creation of vortices occurs on the upper side of the cylinder before the lower side. The first vortex is always shed from the side with higher relative velocity, indicating that the preferred side of cylinder with the first vortex shedding is controlled by the sign of K. Another difference between the K = 0 and $K>0$ cases is the complex vortex structure that occurs in the wake. This structure is a result of the interaction between the constant vorticity embedded in the free stream and the boundary layers at the cylinder wall.

For K = 0.1 (Fig. 2(b)), a Kármán vortex street appears behind the cylinder, indicating that even a small value of K could change a stable flow to an unstable flow when $Re<Re_{crit}$ (Re_{crit} is a critical Reynolds number, the Kármán vortex street with periodic vortex shedding from the cylinder can be detected in the wake when $Re>Re_{crit}$). As K increases to 0.2, the pattern of streaklines is found to be similar as to those for the case when K = 0.1.

When $K\geqslant 0.3$ (Fig. 2(c) and (d)), an important change in the flow is observed. The vortex street observed at $K\leqslant 0.2$ disappears. The separation point on the low side of the cylinder starts at the leading edge. There is a closed recirculation zone which is made up of two opposing asymmetrical vortices attached to the cylinder. The clockwise vortex is larger than that of anticlockwise vortex. The flow pattern is again stable. The present results indicate that for low Reynolds numbers ($Re<Re_{crit}$) flow around a square cylinder, with a small value of K, vortex shedding may be induced. On the other hand, with a large value for K, the vortex shedding is suppressed.

Patterns of instantaneous streaklines for Re = 100 at different values of K is shown in Fig. 3. When K = 0, the flow behind the cylinder is characterized by a Kármán vortex street, which consists of vortices in a regular alternating arrangement. The distance between consecutive vortices remains almost constant. When K = 0.1, periodic vortex

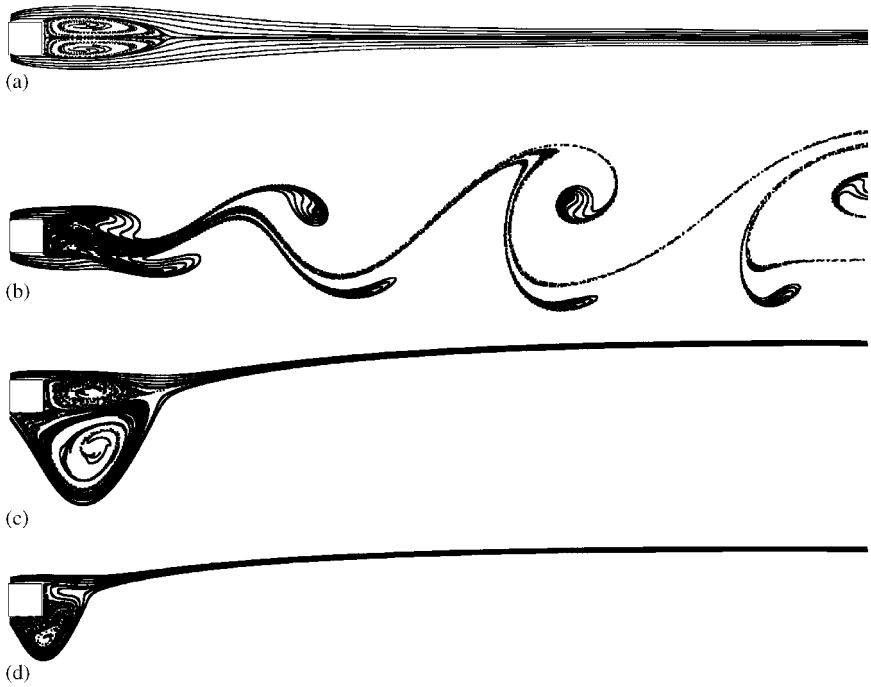

Fig. 2. Patterns of instantaneous streaklines for Re = 50 at different K: (a) K = 0, (b) K = 0.1, (c) K = 0.3, and (d) K = 0.5.

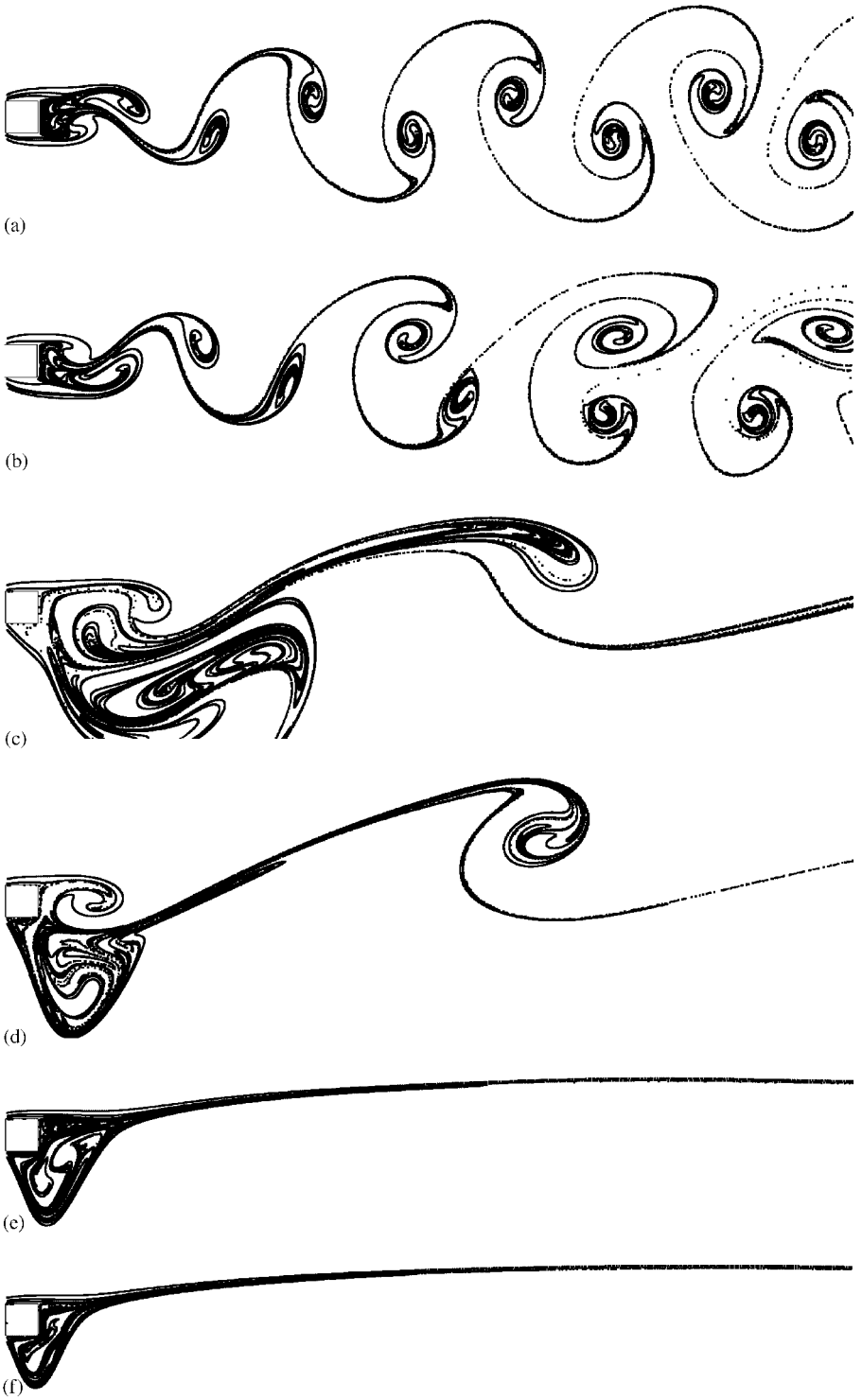

Fig. 3. Patterns of instantaneous streaklines for Re = 100 at different K: (a) K = 0, (b) K = 0.1, (c) K = 0.2, (d) K = 0.3, (e) K = 0.4, and (f) K = 0.5.

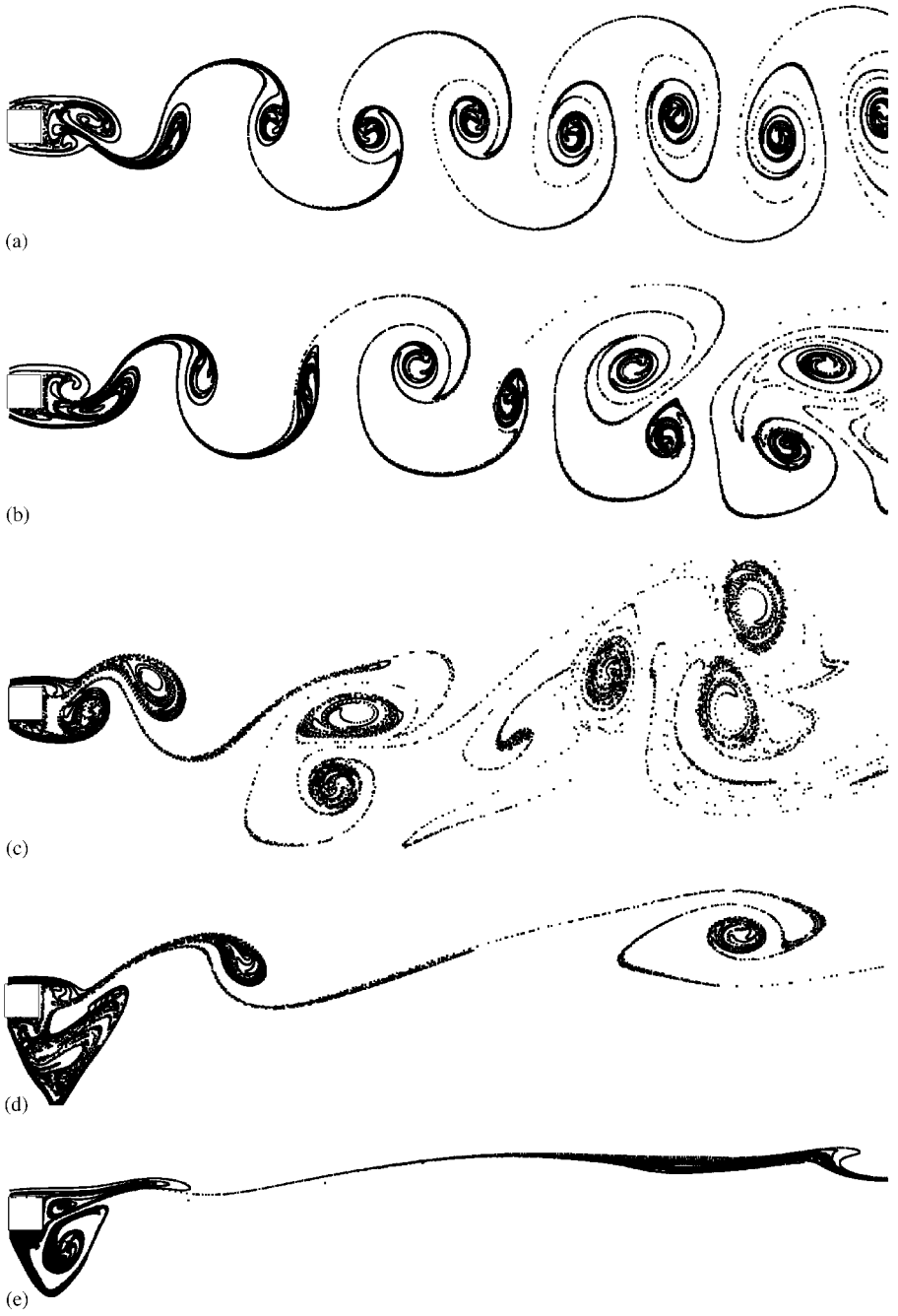

Fig. 4. Patterns of instantaneous streaklines for Re = 200 at different K: (a) K = 0, (b) K = 0.1, (c) K = 0.2, (d) K = 0.4, and (e) K = 0.5.

shedding remains and forms the Kármán vortex street in the wake (Fig. 3(b)). It is noted from Fig. 3(b) that although the vortex street consists of a string of alternately signed vortices which are arranged in two rows, due to the effect of shear flow, the vortices which are shed from the upper wall of the cylinder are larger than those shed from the lower wall. The vortices produced at the lower edge tend to be more elongated and are transported downstream at a slower speed than the fairly round vortices occurring from the upper wall. The interaction between vortices of different intensity leads to a vortex structure with irregular lateral and longitudinal vortex spacing. In addition, the intensity of

vorticity dissipates as vortices produced at the lower edge move downstream. This is expected since the vorticity of the vortex shed from the lower side of the cylinder has the opposite sign to that of the vorticity embedded in the free stream when $K>0$. Thus, the vortex shed from the lower side of the cylinder dissipates faster in shear flow than it does in uniform flow.

The pattern of instantaneous streaklines for $K = 0.2$ is found to be quite different from those in the $K = 0$ and 0.1 cases (see Fig. 3(c)). Vortices are shed from the upper and lower sides of the cylinder, but the regular vortex configuration in the near-wake is destroyed. The size of the formation region of the vortices behind the cylinder is very large. The shapes of alternately shed vortices are round followed by slender ones. This pattern becomes more apparent when $K = 0.3$ (Fig. 3(d)). The most dramatic changes take place in the wake when K is increased further, to 0.4. The flow pattern behind the cylinder is totally different from that in the previous cases. When $K = 0.4$, the formation region of vortices and streakline pattern do not change with time (see Fig. 3(e)). The Kármán vortex street has disappeared completely. The flow pattern does not appear significantly different when $K = 0.5$ (Fig. 3(f)). The present results suggest that when K is greater than a value of about 0.4, the flow pattern approaches a form of self-similarity and a stable flow will ultimately occur.

The patterns of streakline evolution with K for $Re = 200$ are found to be similar to those for $Re = 100$. As K increases, the vortex street with periodic vortex shedding from the cylinder is suppressed. However, comparing Fig. 4 with Fig. 3, one can observe that flow is still unstable at $K = 0.5$ (Fig. 4(e)). It is clear that the flow structure around the cylinder depends on both Re and K. On one hand, flow becomes more unstable as Re increases at a fixed K. On the other hand, the suppression of vortex shedding becomes stronger as K increases with a fixed Reynolds number.

In order to gain further insight into the evolution of vortex shedding in the near-wake region, the patterns of vorticity contours for $Re = 100$ at different K and times are plotted in Figs. 5–9. In these figures the circle symbol represents the position of the front stagnation point, the negative vorticity (clockwise vortex) is shown by dashed lines and the positive vorticity (anticlockwise vortex) by solid lines. The sequence of vorticity contours clearly describes the process of vortex formation and shedding from the cylinder.

In the case of uniform flow ($K = 0$) past the cylinder, the alternating vortices with the same strength and size are shed from the upper and lower side of the cylinder (Fig. 5). The mean position of the front stagnation point is located at the centre of the front surface of the cylinder. At $t = 190$, a positive vortex appears on the lower side of the cylinder and a negative vortex is rolling up on the upper side of the cylinder (Fig. 5(a)). While the negative vortex is being shed at $t = 195$, the positive one on the other side is reforming (Fig. 5(b)). The dimensionless vortex shedding frequency is about 0.145, which is in close agreement with the value of 0.146 reported by Sohankar et al. (1998).

Fig. 6 shows the vorticity contours at different time instants during one cycle of vortex shedding for $K = 0.1$. The process of vortex shedding is similar to that shown for the case of $K = 0$. Fig. 6(a) shows that at $t = 291$, a positive vortex is in the process of development on lower side of the cylinder, while a negative vortex is about to detach from the cylinder. Later in time, $t = 295$ (Fig. 6(c)), the positive vortex draws the shear layer of opposite sign from the upper side of the wake across the wake centreline which eventually cuts the supply of vorticity to the positive vortex ($t = 297$, Fig. 6(d)). Formation of the positive vortex is completed at $t = 299$ (Fig. 6(e)), after which the vortex is transported

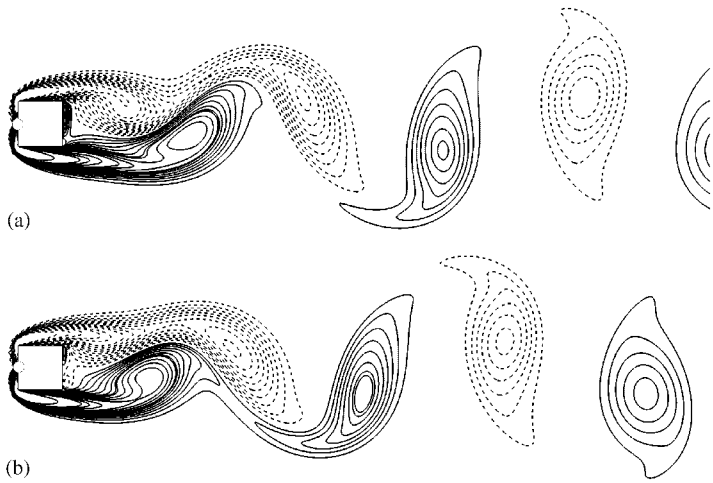

Fig. 5. Vorticity contours at several time instants during half a cycle of vortex shedding for $Re = 100$ and $K = 0$: (a) $t = 190$ and (b) $t = 195$.

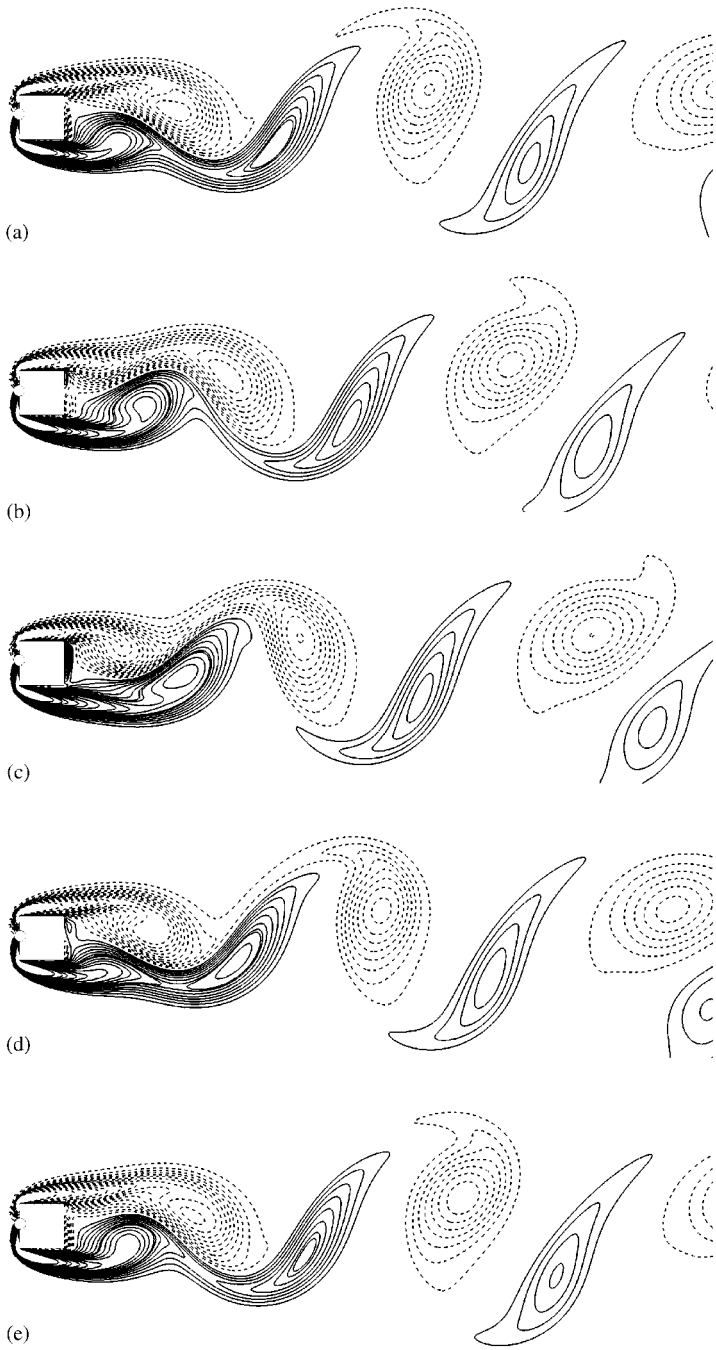

Fig. 6. Vorticity contours at several time instants during one cycle of vortex shedding for Re = 100 and K = 0.1: (a) t = 291, (b) t = 293, (c) t = 295, (d) t = 297, and (e) t = 299.

downstream by the flow field. This evolutionary process is repeated approximately every eight dimensionless time periods. It is observed that the vortices are shed alternately, with positive vortices being oblate in shape and the negative vortices being round. The mean position of the front stagnation point is on the front surface of the cylinder and slightly above the centreline.

When K = 0.2 (Fig. 7), the process of vortex forming and shedding are found to be quite different from those in the K = 0 and 0.1 cases. At t = 100, there are three vortices, a negative vortex and two positive vortices in the region behind

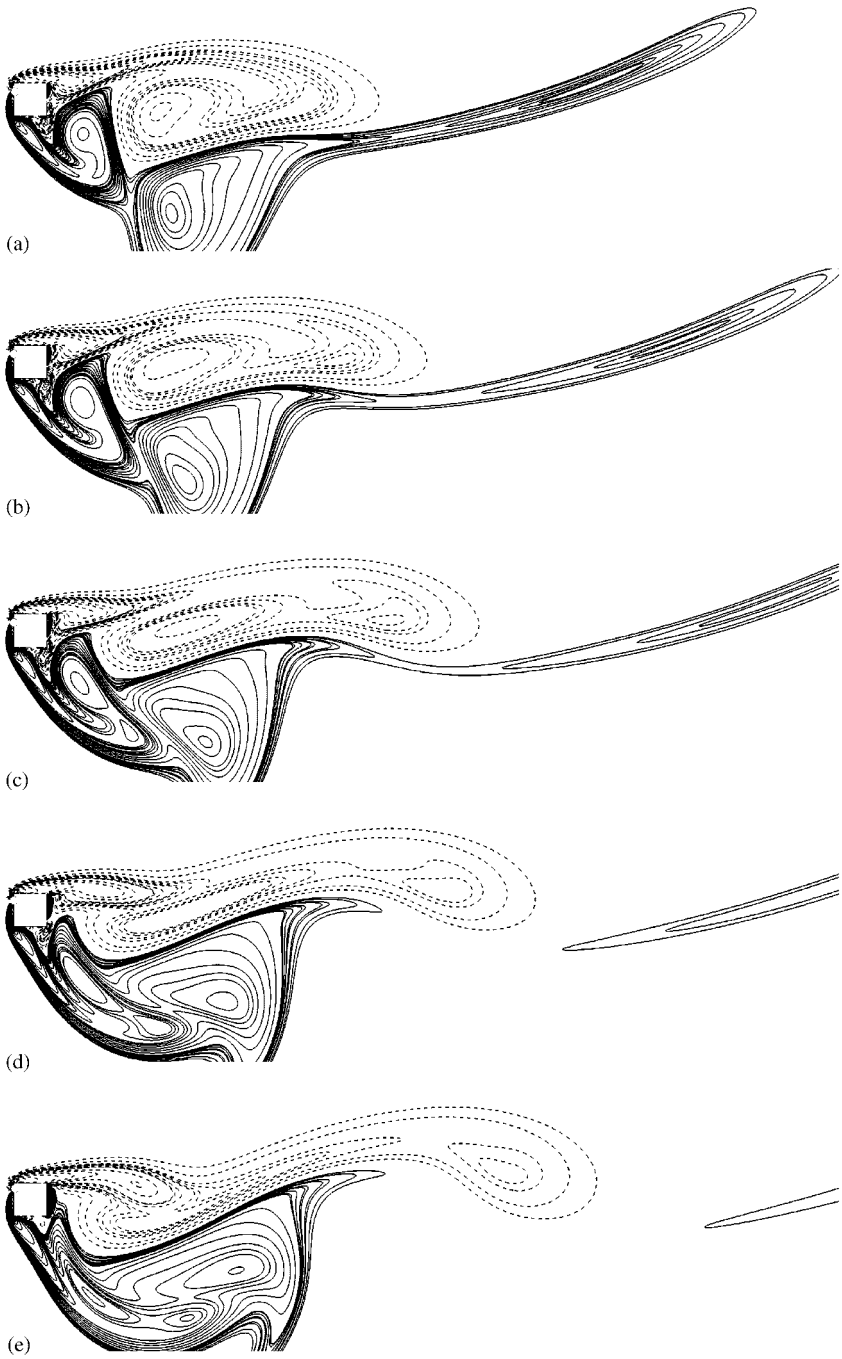

Fig. 7. Vorticity contours at several time instants during one cycle of vortex shedding for Re = 100 and K = 0.2: (a) t = 100, (b) t = 102, (c) t = 104, (d) t = 106, and (e) t = 108.

the cylinder. These vortices of opposite sign are generated from both sides of the cylinder, but they do not detach from the cylinder. This is because, as K increases, the velocity of the free stream on the lower side of the cylinder decreases and even reverses direction, so that the positive vortex that is produced at the lower side of the cylinder cannot be efficiently swept downstream by the free stream. This vortex immediately interacts with the negative vortex which is in the process of being formed on the upper side of the cylinder. The two vortices with opposite sign interact in the near-wake and partially annihilate each other's vorticity. The remaining vorticity is then fed into the neighbouring juvenile

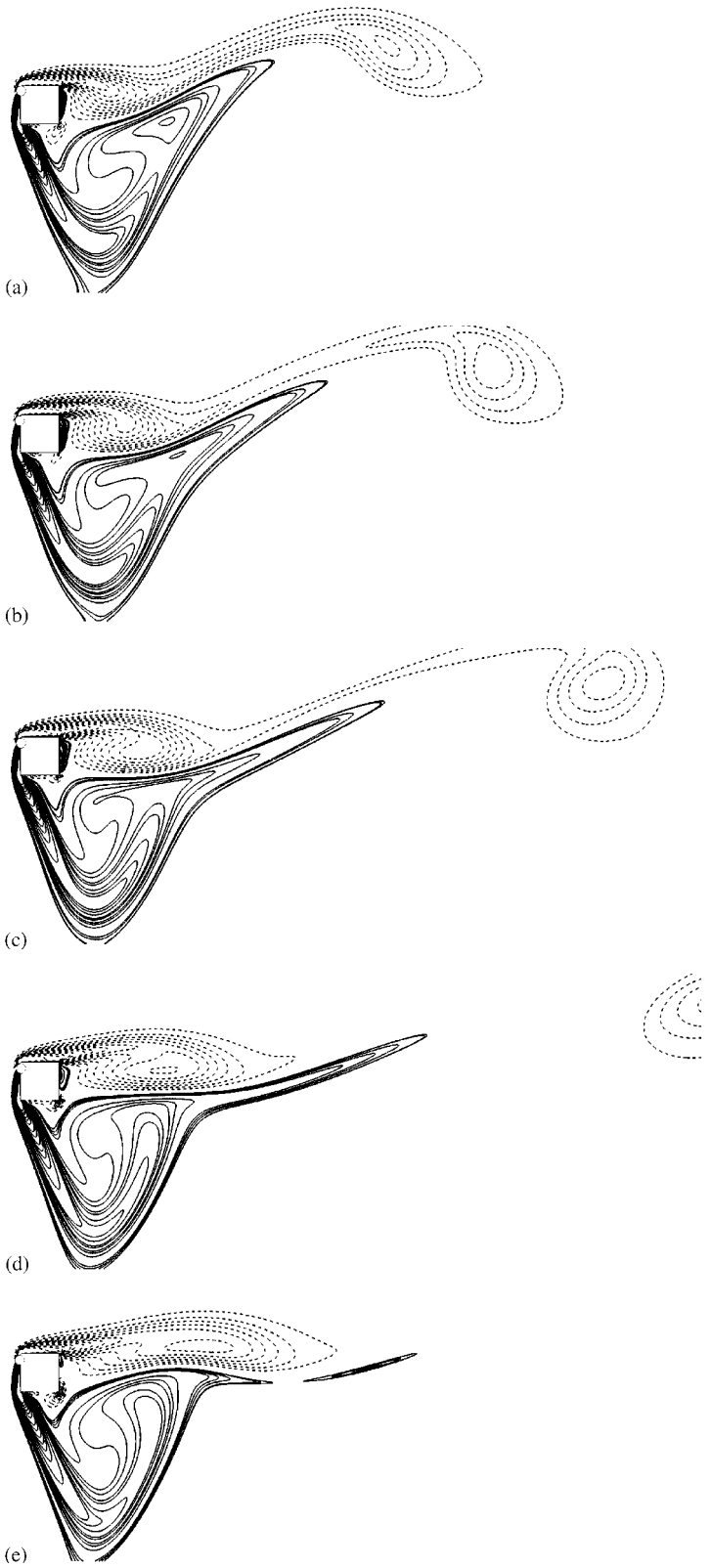

Fig. 8. Vorticity contours at several time instants during one cycle of vortex shedding for Re = 100 and K = 0.3: (a) t = 283, (b) t = 285, (c) t = 287, (d) t = 289, and (e) t = 291.

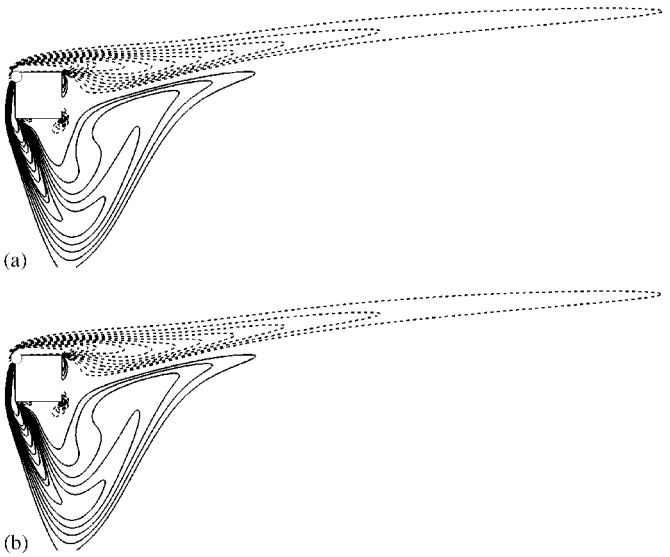

Fig. 9. Vorticity contours for Re = 100 and K = 0.4 at: (a) t = 295, and (b) t = 299.

vortices of identical sign which merge to form stronger vortices. Subsequently, the vortices are swept downstream. The shapes of the vortices shed from the cylinder alternate between round (negative vortices from the upper edge) and slender (positive vortices from the lower edge). The differences in the size and strength of the alternately shed vortices are more pronounced as they travel downstream. It is further noted from Fig. 7 that two interacting vortices with opposite sign in the formation region are significantly distended along the horizontal axis, resulting in a large formation region of vortices behind the cylinder.

Fig. 8 shows the vorticity contours at five time instants during one cycle of vortex shedding at K = 0.3. A positive vortex has appeared on the lower side of the cylinder and a negative vortex has begun to roll up on the upper side of the cylinder at t = 283, while a negative vortex is being shed into wake. It is observed that the formation region of vortices behind the cylinder becomes a triangular zone, and the zone changes with time. As time increases, the negative vortex continues to grow gradually and interacts with the positive vortex. The negative and positive vortices are stretched out by this interaction (Fig. 8(d)). At t = 291, a very weak vortex is separated from the positive vortex. Its core is more elongated, but it is still distinct in the near-wake (Fig. 8(e)). As this vortex is transported downstream, its dissipation rate is greater than that of the negative vortex, and eventually all positive vorticity is dispersed, so that only negative vortices remain and form a single vortex street in the wake slightly further away from the cylinder.

The patterns of instantaneous vorticity contours at K = 0.4 are shown in Fig. 9. It is interesting to note that in the present case the periodic flow pattern does not develop with time and the positive vortex and negative vortex are shed at the same time. In other words, the negative vortices shed engulf and neutralize the positive vortices. The process by which the vortices are shed from the square cylinder is completely different to that for $K \leqslant 0.3$, and the vortices are only shed from the upper shear layer. The formation region of the vortices and vorticity contour pattern do not change with time. It is found that the front stagnation point is located at the left top corner of the cylinder.

The variation of mean position of the stagnation point on the front face of the cylinder with the shear rate K for different Re is plotted in Fig. 10. The position of the stagnation point is at the centre point on the front face when K = 0. As K increases, the stagnation point shifts from the centre point towards the left top corner of the cylinder, resulting in the increase of the area of the formation region of the vortices on the lower side of the cylinder. When $K > 0.3$, the stagnation point remains in the vicinity of the corner, thus a triangular zone is formed under the cylinder. If the variation of the stagnation point with K at Re = 50 is compared with that at Re = 100, one will find the former increases at a faster rate that the latter.

3.2. Forces

Fig. 11 shows the time-averaged pressure (C_{Pav}) distribution on the surface of the cylinder ($C_{Pav} = (1/T)\int_0^T C_P\,dt$, where T is the time). Here, the effects of shear rate and Reynolds number are clearly revealed. Fig. 11(a) shows the

distribution for Re = 100 at different K. The distribution at K = 0 is observed to be symmetric. The maximum value of the pressure on the surface of the cylinder is at the centre point of the front face. The distribution at K = 0.1 is very similar to the case of K = 0. When K > 0.1, however, the pressure distribution is significantly different. On the front face (A–B), there is a distinct shift in the location of the maximum pressure as K increases—from the centre point of the face towards the top left corner of the cylinder. When K = 0.5, the pressure approaches a nearly linear distribution on the front face. The changes in the pressure distribution on the other surfaces are relatively small in comparison to those seen on A–B. The mean pressure value on these surfaces is approximately a constant for K > 0.2. The tendency towards similarity in pressure at K = 0.3, 0.4 and 0.5 also supports the argument that the flow structure approaches a form of self-similarity. In addition, the pressure drop between the front and rear face of the cylinder at K = 0 is larger than that at K = 0.5, indicating that the drag force decreases with the increase of K. Fig. 11(b) shows the pressure distribution on each face for different Re and K = 0.3. It is observed that the pressure difference between on the front and on the back surface of the cylinder is reduced as Re is increased. Hence we conclude that the drag force on the cylinder will decrease with any increase of Re.

The lift and drag coefficients, C_L and C_D, experienced by the cylinder have been calculated by integration of the wall pressure and wall shear stress on the cylinder surface. The time histories of these coefficients are plotted in Figs. 12–14. In the case of Re = 50, the lift and drag coefficients are constants at K = 0 (Fig. 12(a)). This is related to the stable wake flow in Fig. 2(a). When K = 0.1, the lift and drag coefficients exhibit a regular fluctuations (Fig. 12(b)). This is related to alternate vortex shedding. As K increases to 0.2, the fluctuation magnitude increases (Fig. 12(c)). When K ⩾ 0.3, however, the fluctuation disappears (Fig. 12(d)). The lift and drag coefficients become constants again which is

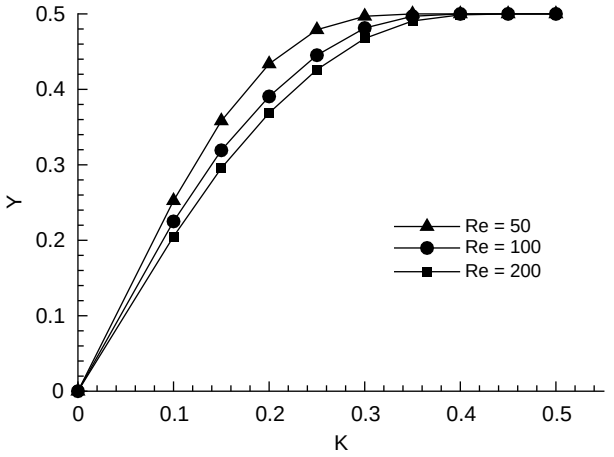

Fig. 10. Variation of the stagnation point with K.

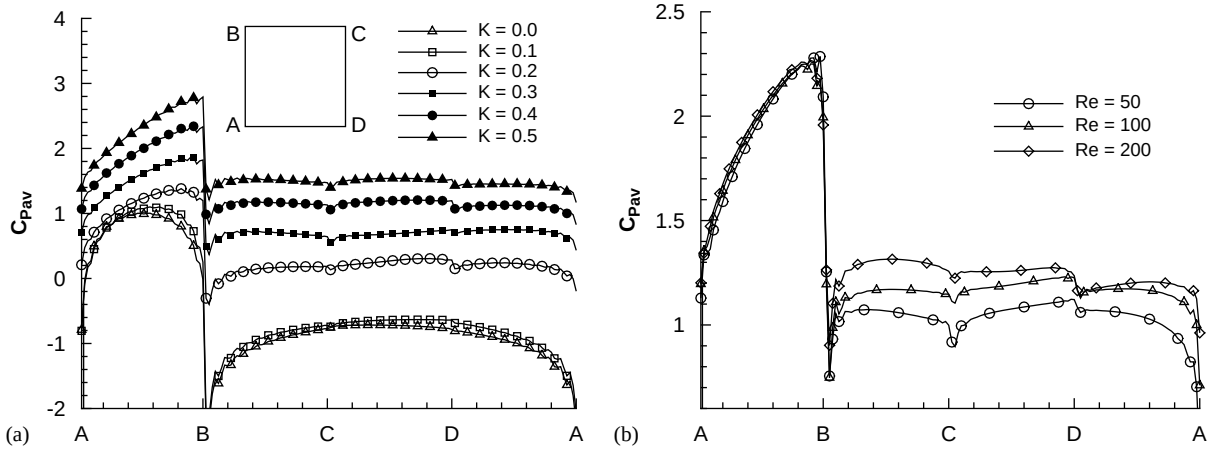

Fig. 11. Mean pressure distribution on the surface of the cylinder: (a) Re = 100 at different K and (b) K = 0.3 for different Re.

consistent with the stable wake flow seen for cases where $K \geqslant 0.3$ (see Fig. 2(c) and (d)). Comparing Fig. 12(d) with Fig. 12(a), one can observe that the lift and drag coefficients decrease from 1.5 to 0.82 and from 0 to −0.15.

Fig. 13 shows the time histories of the lift and drag coefficients for $Re = 100$. When $K = 0$, the lift and drag coefficients show regular fluctuations with an approximately constant amplitude except at the early stages of the flow. It is clear that the periodic fluctuation is related to alternate vortex shedding (Fig. 3(a)). The amplitude of periodic fluctuation in the lift and drag coefficients slightly increases at $K = 0.1$. The drag coefficient fluctuates at twice the frequency of the lift coefficient and one of the peaks of fluctuation is more pronounced than the other one, since the two oppositely signed vortices shed per cycle are different in strength. When $K = 0.2$ (Fig. 13(c)), the lift and drag signals are still periodic but exhibit irregular characteristics. This could be related to an unstable transition which occurs in the near wake. As K increases to 0.3 (Fig. 13(d)), regular C_L and C_D fluctuate periodically again, however the drag coefficient fluctuates at the same frequency as the lift coefficient, and the frequency is lower than that of $K = 0$ or 0.1. When $K = 0.4$, the lift and drag coefficients almost become straight lines. This is related to the stable wake flow seen in Fig. 3(e).

The time histories of the lift and drag coefficients for $Re = 200$ is shown in Fig. 14. Comparing Fig. 14 with Fig. 13, one can observe that the periodic fluctuation pattern of the lift and drag coefficient is basically the same at $K = 0$ and 0.1, but the magnitude of fluctuation for $Re = 200$ is larger than that for $Re = 100$. When $K = 0.4$, the magnitude of fluctuation for $Re = 200$ reduces remarkably, but does not attain a constant as vortices continue to be shed (Fig. 4(d)).

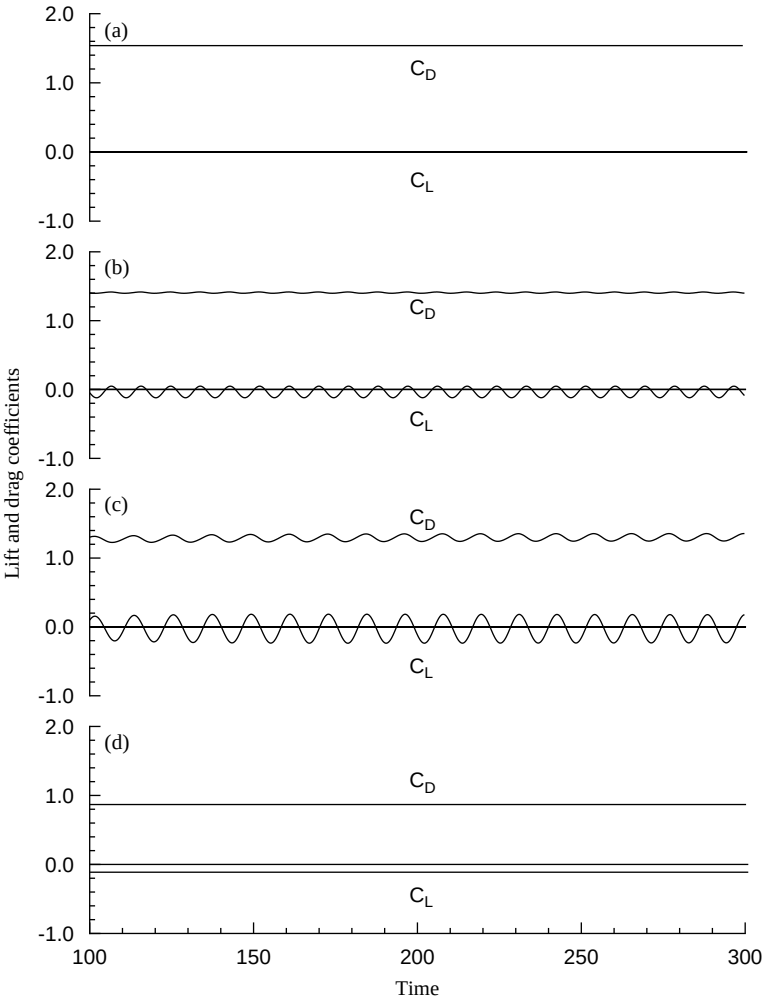

Fig. 12. Variation of the lift and drag coefficients with time for $Re = 50$ at different K: (a) $K = 0$, (b) $K = 0.1$, (c) $K = 0.2$, and (d) $K = 0.3$.

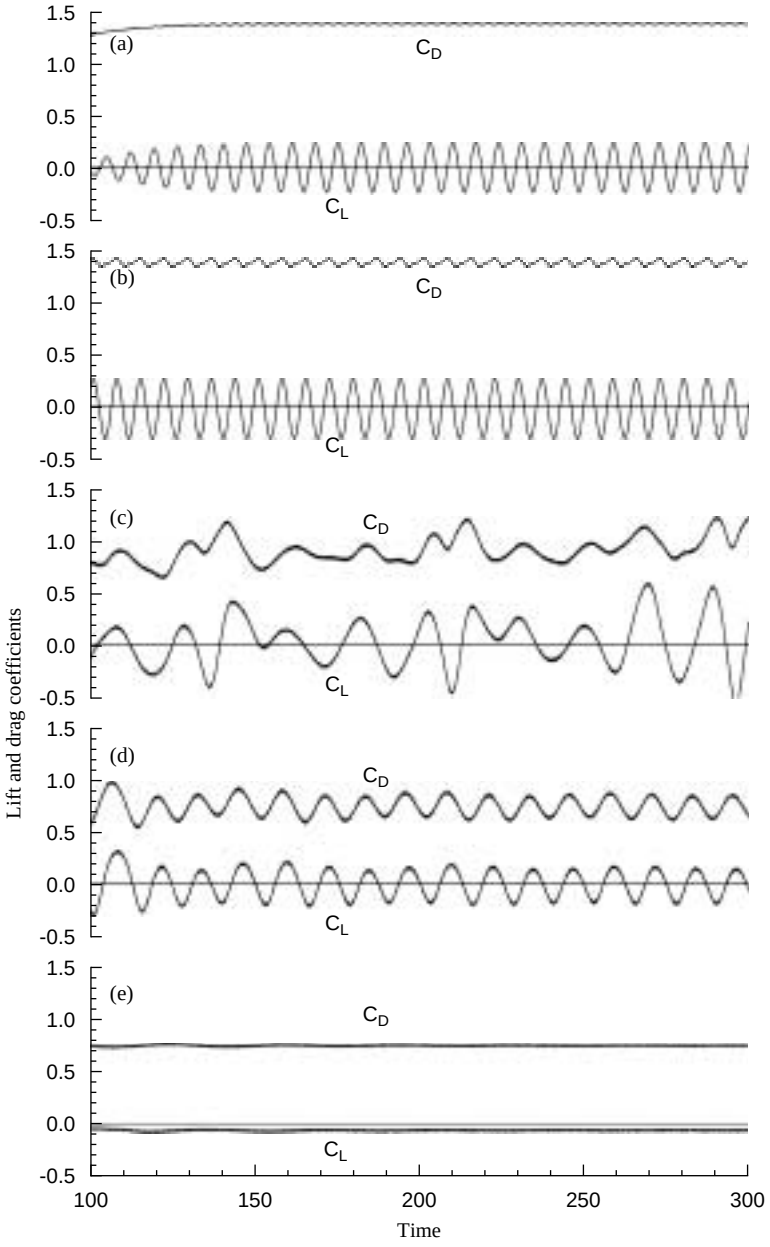

Fig. 13. Variation of the lift and drag coefficients with time for $Re = 100$ at different K: (a) $K = 0$, (b) $K = 0.1$, (c) $K = 0.2$, (d) $K = 0.3$, and (e) $K = 0.4$.

The vortex shedding frequencies are estimated from power spectra of the lift coefficients C_L. Fig. 15 shows the power spectra for various values of K where $Re = 100$. When $K = 0$ and 0.1, there is one prominent frequency in the lift spectrum; their values are 0.145 at $K = 0$ and 0.143 at $K = 0.1$, respectively. More than one peak is observed in the power spectrum when $K = 0.2$ and 0.3, and the most dominant frequency is 0.06 and 0.075, respectively. This indicates that the vortex shedding process is more complex for K in this range than for low-K flow. When $K = 0.4$, the estimated domain is close to zero, indicative of stable wake flow (i.e. an infinite period for vortex shedding). The present results show that the vortex shedding frequency, in general, decreases with increasing K for a square cylinder. This behaviour is different from the results of shear flow past a circular cylinder (Kiya et al., 1980).

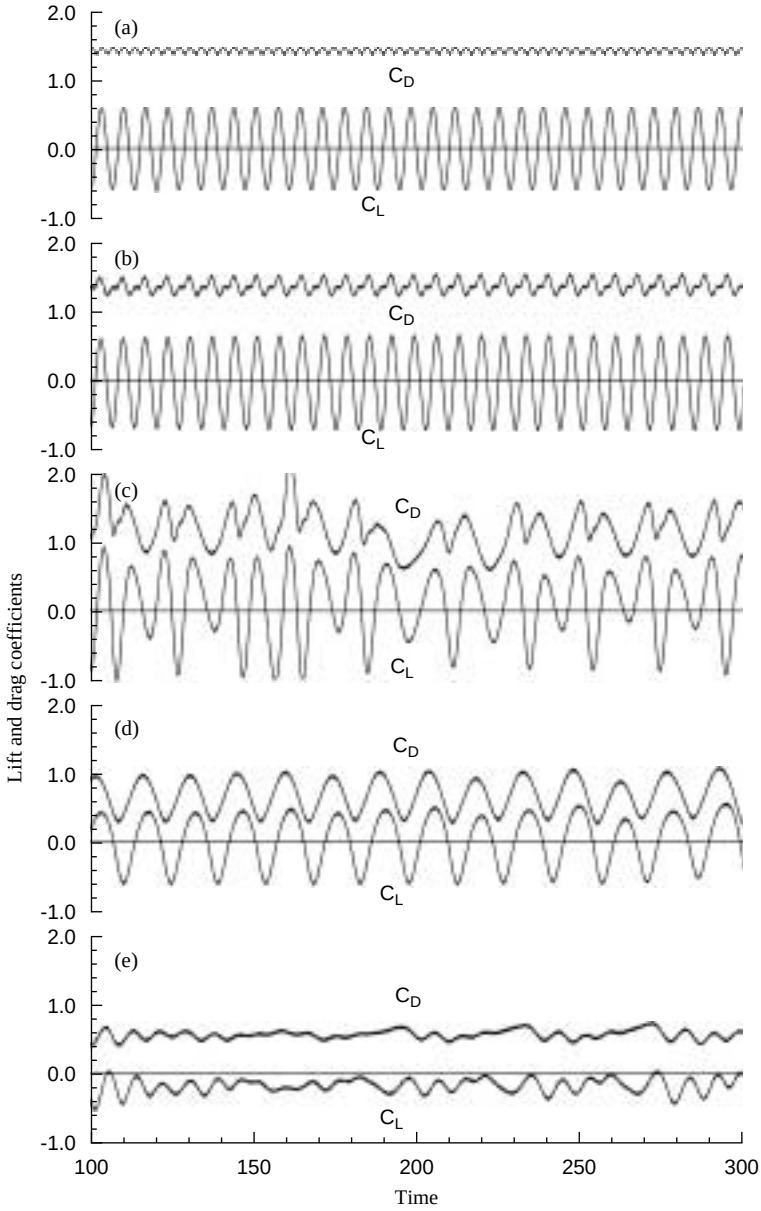

Fig. 14. Variation of the lift and drag coefficients with time for Re = 200 at different K: (a) K = 0, (b) K = 0.1, (c) K = 0.2, (d) K = 0.3, and (e) K = 0.4.

The variations of the time-averaged lift and drag coefficients with K are plotted in Fig. 16. As the shear rate increases, the mean drag coefficient decreases; for example, when Re = 100, K = 0, 0.1, 0.2, 0.4 and 0.5, the mean values of the drag coefficients are about 1.42, 1.36, 0.9, 0.73 and 0.73, respectively. This behaviour is in agreement with the experimental results of Kwon et al. (1992) for shear flow past a circular cylinder. However, the present results also show that with an increase in Reynolds number there is a reduction in the lift and drag coefficients. When K increases from 0 to 0.5, the mean value of the drag coefficient can be reduced by up to 50%. It is worth noting that a substantial reduction of the mean drag occurs in the range $0.15<K<0.3$. When $K>0.3$, the reduction in C_{Dav} becomes insignificant. On the other hand, the mean value of the lift coefficient is rather insensitive to changes of K. Hence, the effect of shear rate on the lift force seems to be fairly small within the range of the present simulations, while the drag coefficient is affected greatly by the shear rate.

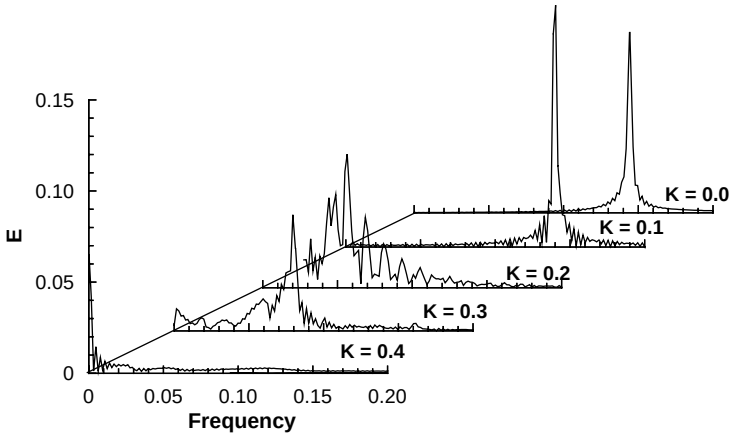

Fig. 15. Power spectrum of lift forces acting on the cylinder against K for Re = 100.

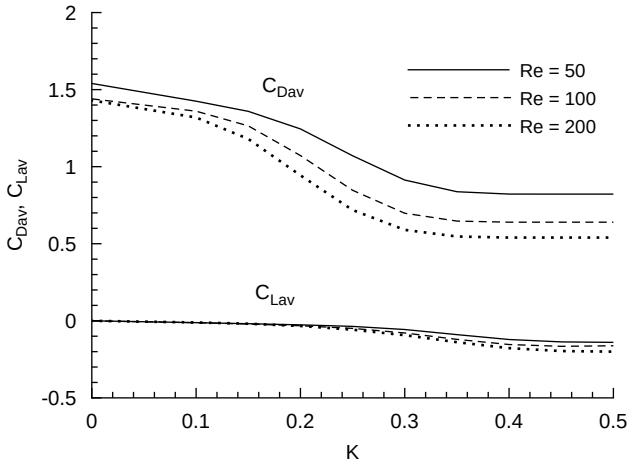

Fig. 16. Effect of shear rate K on the mean value of the lift and drag coefficients.

4. Conclusion

This paper has reported the results of lattice Boltzmann simulations of incompressible, linear-shear flow past a square cylinder at Re = 50, 100 and 200. The present simulation provides some novel and important information regarding flow in the wake behind a square cylinder at different shear rates. It is found that the vortex shedding and wake development behind the cylinder are significantly dependant on both the magnitude of the shear rate K and the Reynolds number Re. When $Re > 50$, as K increases, the formation region of the vortices behind the cylinder shifts to the lower side of the cylinder and forms a triangular region, while the stagnation point on the front face of the cylinder moves towards the left top corner. The differences in the size and strength of the alternately shed vortices become more pronounced with increasing K. The shapes of alternatively shed vortices are round followed by slender ones. As these vortices travel downstream, the slender vortices dissipate at a higher rate than the round vortices, and eventually disappear, so that only the round vortices remain and form a single vortex street in the far wake. When K is greater than a critical value, which depends on the Reynolds number, the vortex street completely disappears and flow becomes a stable state. Under the same conditions, flow structure and pressure distribution around the cylinder tend towards self-similarity with increasing K. When $Re = 50 < Re_{crit}$, a small K can disturb the steady state and cause alternate vortex shedding from the cylinder, resulting in an unsteady wake flow. However, as K increases to a certain value, the wake flow becomes steady again.

The results presented here show that the lift and drag forces exerted on the cylinder, in general, decrease with increasing K and Re. The reduction in the drag force follows the same trend observed by Kwon et al. (1992) for a shear flow past a circular cylinder, but the vortex shedding frequency, in general, decreases with increasing K. This behaviour is different from the results of shear flow past a circular cylinder. It is found that the effect of shear rate on the lift force seems to be fairly small in the range of the present simulations, while the drag coefficient is affected greatly by the shear rate. When K increases from 0 to 0.5, the mean value of the drag coefficient can be reduced by up to 50%. It is found that the decreasing rate of the drag force is most distinct in the range $0.15<K<0.3$.

References

Ansumali, S., Chikatamarla, S.S., Frouzakis, C.E., Boulouchos, K., 2004. Entropic lattice Boltzmann simulation of the flow past square cylinder. International Journal of Modern Physics C 15, 435–445.

Ayukawa, K., Ochi, J., Kawahara, G., Hirao, T., 1993. Effect of shear rate on the flow around a square cylinder in a uniform shear flow. Journal of Wind Engineering and Industrial Aerodynamics 50, 97–106.

Benzi, R., Succi, S., Vergassola, M., 1992. The lattice Boltzmann equation: theory and applications. Physics Reports 222, 145–197.

Bhatnagar, P.L., Gross, E.P., Krook, M., 1954. A model for collision processes in gases. I. Small amplitude processes in charged and neutral one-component system. Physics Review 94, 511–525.

Chapman, S., Cowling, T.G., 1970. The Mathematical Theory of Non-uniform Gases. Cambridge University Press, Cambridge.

Chen, S., Doolen, G.D., 1998. Lattice Boltzmann method for fluid flows. Annual Review of Fluid Mechanics 30, 329–364.

Cheng, M., Hung, K.C., 2004. Lattice Boltzmann method on non-uniform mesh. International Journal of Computational Engineering and Science 5, 291–302.

Cheng, M., Hung, K.C., 2006. Vortex structure of steady flow in a rectangular cavity, Computers & Fluids 35, 1046–1062.

Cheng, M., Tan, S.H.N., Hung, K.C., 2005. Linear shear flow over a square cylinder at low Reynolds number. Physics of Fluids 17, 078103.

Davis, R.W., Moore, E.F., 1982. A numerical study of vortex shedding from rectangles. Journal of Fluid Mechanics 116, 475–506.

Gallivan, M.A., Noble, D.R., Georgiadis, J.G., Buckius, R.O., 1997. A evaluation of the bounce-back boundary condition for lattice Boltzmann simulations. International Journal for Numerical Methods in Fluids 25, 249–263.

He, X., Luo, L.S., Dembo, M., 1996. Some progress in Lattice Boltzmann method. Part I. Nonuniform mesh grids. Journal of Computational Physics 129, 357–363.

He, X., Zou, Q., Luo, L.S., Dembo, M., 1997. Analytic solutions of simple flow and analysis of non-slip boundary conditions for the lattice Boltzmann BGK model. Journal of Statistical Physics 87, 115–136.

Higuera, F., Jimenez, J., 1989. Boltzmann approach to lattice gas simulations. Europhysics Letters 9, 663–668.

Higuera, F., Succi, S., Benzi, R., 1989. Lattice gas dynamics with enhanced collisions. Europhysics Letters 9, 345–349.

Inamuro, T., Yoshino, M., Ogino, F., 1995. A non-slip boundary condition for lattice Boltzmann simulations. Physics of Fluids 7, 2928–2930.

Jan, Y.J., Sheu, W.H., 2004. A numerical configuration of the dual body vortex flowmeter design. Computers and Fluids 33, 1157–1174.

Jordan, S.K., Fromm, J.E., 1972. Laminar flow past a circle in a shear flow. Physics of Fluids 15, 972–976.

Kiya, M., Tamura, H., Arie, M., 1980. Vortex shedding from a circular cylinder in moderate-Reynolds number shear flow. Journal of Fluid Mechanics 101, 721–735.

Kwon, T.S., Sung, H.J., Hyun, J.M., 1992. Experimental investigation of uniform-shear flow past a circular cylinder. ASME Journal of Fluids Engineering 114, 457–460.

Ladd, A.J.C., 1994. Numerical simulation of particulate suspensions via a discretized Boltzmann equation. Part.1. theoretical foundation. Journal of Fluid Mechanics 271, 285–309.

Nannelli, F., Succi, S., 1992. The lattice Boltzmann equation on irregular lattices. Journal of Statistical Physics 68, 401–407.

Noble, D.R., Chen, S., Georgiadis, J.G., Buckius, R.O., 1995. A consistent hydrodynamic boundary condition for the lattice Boltzmann method. Physics of Fluids 7, 203–209.

Okajima, A., 1982. Strouhal number of rectangular cylinder. Journal of Fluid Mechanics 123, 379–398.

Rossi, N., Ubertini, S., Bella, G., Succi, S., 2005. Unstructured lattice Boltzmann method in three dimensions. International Journal for Numerical Methods in Fluids 49, 619–633.

Sohankar, A., Norberg, C., Davidson, L., 1998. Low-Reynolds number flow around a square cylinder at incidence: study of blockage, onset of vortex shedding and outlet boundary condition. International Journal for Numerical Methods in Fluids 26, 39–56.

Succi, S., 2001. The Lattice Boltzmann Equation for Fluid Dynamics and Beyond. Oxford University Press, Oxford.

Sung, H.J., Chun, C.K., Hyun, J.M., 1995. Experimental study of uniform-shear flow past a rotating cylinder. ASME Journal of Fluids Engineering 117, 62–67.

Wolf-Gladrow, D.A., 2000. Lattice-Gas Cellular Automata and Lattice Boltzmann Models: An Introduction. Lecture Notes in Mathematics, No.1725. Springer, New York.

Zhou, L., Cheng, M., Hung, K.C., 2005. Suppression of fluid on a square cylinder by flow control. Journal of Fluids and Structures 21, 151–167.

Ziegler, D.P., 1993. Boundary conditions for lattice Boltzmann simulations. Journal of Statistical Physics 71, 1171–1177.